Numerical Study on Hydrodynamics of Short-Dwell Paper Coaters

Zhenlei Cao and M. Nabil Esmail
Dept. of Chemical Engineering, University of Saskatchewan, Saskatoon, Saskatchewan, S7N 0W0 Canada

The influence of flow hydrodynamics is studied numerically on the operating parameters of short-dwell paper coaters. The flow in and around a coater is numerically simulated using the method of finite difference, body-fitted numerical grid generation, and a new computational technique for the solution of viscous incompressible Navier – Stokes equations. The results reflect a simultaneous solution of the problem in and around the coating pond. The computational strategy includes the treatment of mathematical singularities at dynamic and static contact points, and the boundary conditions at free surfaces with stagnation points. A dynamic contact angle is calculated simultaneously with the solution. Results include shear rate, centrifugal force, pressure, and velocity distributions in the flow field related to the operating parameters of the coater, the quality of product, and the efficiency of operation.

Introduction

The purpose of paper-coating processes is to provide uncoated paper with certain desirable properties that are required for the particular uses of the paper product. There are pigment-coating processes and functional-coating processes. Pigment coating is applied to uncoated paper to improve its printability and appearance characteristics. It provides a product surface that is more uniform and more receptive to printing ink than the uncoated paper surface. It also enhances the reproduction of graphics and pictures, and improves the color print quality, which is particularly important for multiple color printings. Functional coating is applied to uncoated paper to provide different functional properties to satisfy certain uses of the products. They may be designed to produce thermosensitive recording paper for facsimile machines and other thermorecording devices. Pressure-sensitive noncarbon recording paper is produced by a functional coating process for the purpose of noncarbon copying. Although functional-coating processes are as important as pigment processes, the volume of their products is much smaller than the volume of pigment-coated printing paper. Coating methods used in functional coating are essentially the same methods that are used in pigment coating. In this study we focus our attention on a pigment-coating process.

The coating mixture applied to the paper surface in a pigment-coating process is known as the coating color. The main components of a coating color are pigment, whose content is about 80% by weight, and binders, which are about 20% by weight. The coating color contains minute amounts of other additives. These components are dispersed into water by a high-power agitator. The pigment most commonly used is mainly composed of plate-shaped china clay. However, in some cases calcium carbonate, titanium dioxide, and other pigments are added as copigments. Particle sizes in all pigments are very small. For instance, 80% of particles in the #2 America Clay pigment are less than 2 μm in size. Binders used in color compositions are commonly classified as synthetic or natural binders. The dominant synthetic coating binder is styrene-butadiene latex. Other commonly used synthetic binders are polyvinyl acetate latex and acrylic emulsions. Modified starches are the most popular binders in the natural category. The color properties depend on their composition. According to Kurath (1992), the coating color based on styrene-butadiene latex shows Newtonian behavior even at high shear rates, while coating colors based on starch show non-Newtonian behavior with shear-thinning properties.

In brief, the coating solution or color is in fact a two-phase solid/liquid fluid. The solid particles are extremely tiny, and are present in very high concentrations. If starch is used as a binding agent, the solution may be considered a single-phase non-Newtonian fluid. If the binder is a latex, the coating color is a single-phase Newtonian fluid.

A coating process is primarily designed for the purpose of

Correspondence concerning this article should be addressed to M. N. Esmail.

depositing a uniform thin layer of the coating color over the surface of the uncoated paper, which may be called the substrate or the web. The thickness of the coating layer is usually a few microns. In industrial applications the coating thickness is measured by the weight of coating color, spread over a unit area of the substrate, and is called the coating weight. In pigment coating the coating weight is commonly in the range of 5 to 30 g/m^2. Paper-coating is handled in huge machines, where paper sheets that are a few meters wide roll at speeds up to 30 m/s over a cylinder whose diameter is about one meter. The coating color is applied from attachments to the cylinder. Paper-coating techniques differ in the design of the attached coating color applicator.

Over the past several decades the growth in demand for writing and printing quality paper has outstripped the total growth in demand for paper products. There has been tremendous growth in the production of coated paper. High profit margins in the production of coated paper provided the industry with strong stimulus to improve quality and increase production. Improvements were sought in the materials used in coating, in their compositions, and in the design of more effective coating processes that enhance the quality of the product. The trend in recent developments of paper-coating processes has been toward higher productivity and lower coating weight, while maintaining or improving quality. The dominant method in paper pigment coating is the blade coating method. However, the roll-and-air-knife coating processes are still used to some extent in industry. So far the flooded blade coater is still the most dominant coater currently used in the paper-coating industry. Because the concentration of solid particles in the coating color is very high, any loss of liquid during application will dramatically increase the viscosity and change other rheological properties of the color. If the color loses too much liquid during application, then the quality of the coating will be seriously damaged, and the operation will possibly be disrupted by breakage in the substrate. Breakage is usually due to the high concentration of solid particles combined with blade pressure.

In the mid-1980s, a new design of blade coaters, named short-dwell coaters, was introduced to the coating industry (Wight, 1988). In a short-dwell coater (Figure 1a), the supply system of the coating color and the doctor system are compacted together to form the so-called coating head. The coating head is located under a rubber-covered backing roll, whose diameter is similar to the diameter of a backing roll in a blade coater with roll applicator. The substrate is moving over this backing roll. There is an inlet at the bottom of the coating pond, an overflow baffle on the upstream side of the coating pond, and a doctor blade on the downstream side. The size of the coating pond is about 4 cm in width. Therefore, as is implied by its name, a short-dwell coater dramatically decreases the contact time between the coating color and web during application. As a result, liquid penetration is minimal. In return, a coating operation with high speed, low coating weight, and fewer substrate breaks can be achieved. Sollinger (1989) discussed the main differences between the flooded-nip blade coater and a short-dwell coater. He concluded that the contact time between the coating color and web during application is one order of magnitude shorter for a short-dwell coater. It has been reported (McDermott, 1986; Pentti, 1984) that short-dwell coaters require lower operating

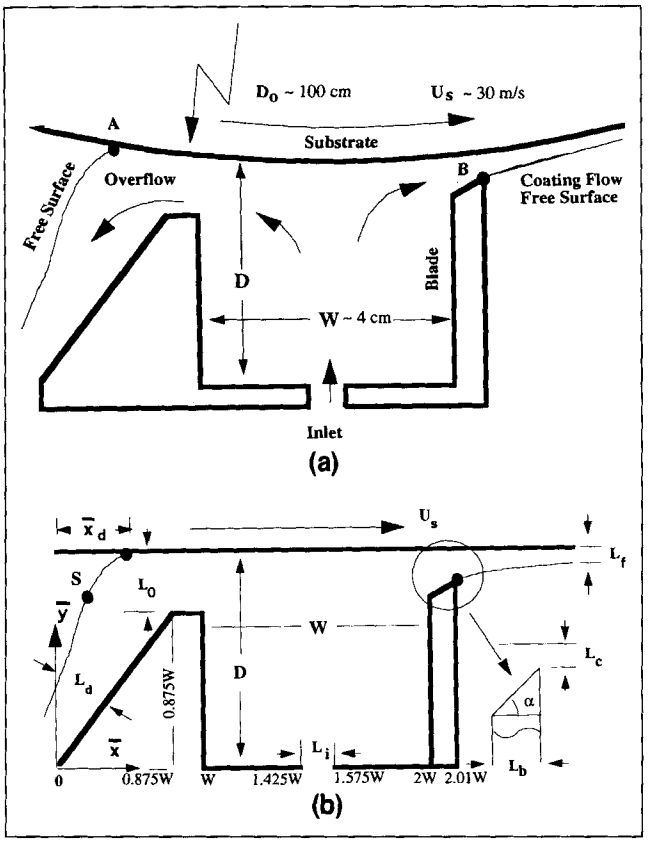

Figure 1. Short-dwell coating process.

(a) A physical process; (b) the physical simulation domain.

pressures applied to the blade and have fewer breaks in comparison to their flooded-nip blade counterparts. It is also found that they can operate at higher speeds and with lower coating weights. Unfortunately, the properties of paper coated in a short-dwell coating operation seem to be poorer. Renvall et al. (1990) found that the paper coated by short-dwell coaters always had lower surface strength and lower gloss, in comparison with paper coated by a blade coater with roll applicators. Moreover, the uniformity of coating weight produced by short-dwell coaters was also poor.

Short-dwell coaters have been in use for less than a decade. It is still a new technology. This process is not well understood, and has not reached its full potential. The unpredictability of operation, nonuniformity of coating weight, and the relatively poor quality of coated products are the main shortcomings of this process. In order to modify the process, the causes of these main shortcomings have to be fully understood. Since the hydrodynamic parameters of this coating process have not been fully investigated yet, an intensive study on the hydrodynamics is much needed to provide some basic theoretical and experimental knowledge of this process.

Previous numerical work either omitted the flow under the blade (Triantafillopoulos et al., 1988), or replaced it by a mathematical sink point. In fact the coating flow has a significant effect on pressure distributions inside the pond (Cao and Esmail, 1992), and an accurate picture of the hydrodynamic parameters could emerge only from the simultaneous interlocked solution of all flows in the domain. In all the previous

publications, the overflow region of the coater was either replaced by an outlet with a parabolic velocity distribution (Triantafillopoulos et al., 1988), or by a channel flow (Cao and Esmail, 1992). These were done to avoid complications associated with the overflow free surface, including a dynamic contact angle and a free surface that can experience surface wavy regimes. In industrial applications the overflow region starts with a channel flow leading from the upstream end of the coating pond to a falling film flow. There is a dynamic contact point (point A, Figure 1a) at the intersection of the free surface and the moving substrate, and a stagnation point on the free surface (point S) as described in Figure 1b.

In this study, a combined method of a finite-difference technique and a body-fitted numerical grid transformation is used to simulate the flow in and around the short-dwell coating pond. The complicated flow region has been simultaneously simulated. It included the flow inside the coating pond, the flow under the blade, the coating flow, and the overflow. The simultaneous solution of the entire flow field allowed total interaction between different flow sections with vastly different geometrical scales. It also allowed the calculation of absolute pressure distributions, since it related the pressure inside the pond to atmospheric pressure at the free surfaces. A comprehensive set of computational results is presented in this article. A full description of all flow parameters, including velocity, pressure, centrifugal force, and shear rate distributions, is reported. The most important aspect of the results is the interaction of these parameters in various regions of the short-dwell coating flow. Other effects of these parameters on the coating operation and coating quality are also addressed.

Formulation and Methods of Solution

A typical short-dwell coater is shown in Figure 1a. The coating liquid flows from the inlet into the pond. The substrate, which is shearing the flow at the top, entrains a coating weight (layer) through the coating gap, under the blade, to leave the section coated by a thin layer with a free surface. The excess liquid, which we call the overflow, moves through a baffle gap and leaves the pond flowing over an inclined surface. The objective of the study was to numerically simulate the flow just described. There are, however, several complicating factors in the simulation. First, the flows inside the pond (about 4 cm) and under the blade (about 0.002 cm) have vastly different geometrical scales. The second factor is the coating free surface and the associated static contact point. Another factor is the overflow free surface and the associated dynamic contact point and stagnation point.

The flow of Newtonian incompressible fluid is governed by the Navier–Stokes equations and the continuity equation. In Cartesian coordinates, the dimensionless conservative form of these equations are

$$\frac{\partial u}{\partial t}+\frac{\partial u^2}{\partial x}+\frac{\partial uv}{\partial y}+\frac{\partial p}{\partial x}=\frac{1}{Re}\left(\frac{\partial^2 u}{\partial x^2}+\frac{\partial^2 u}{\partial y^2}\right) \tag{1}$$

$$\frac{\partial v}{\partial t}+\frac{\partial uv}{\partial x}+\frac{\partial v^2}{\partial y}+\frac{\partial p}{\partial y}=\frac{1}{Re}\left(\frac{\partial^2 v}{\partial x^2}+\frac{\partial^2 v}{\partial y^2}\right)-\frac{1}{Fr^2} \tag{2}$$

$$\frac{\partial u}{\partial x}+\frac{\partial v}{\partial y}=0. \tag{3}$$

In Eqs. 1–3 the characteristic velocity is the substrate speed U_s, the characteristic length is the pond width W, the characteristic time is U_s/W, and the characteristic pressure is ρU_s^2. The dimensionless velocity components in the x and y directions are u and v, respectively; ρ and μ are the density and viscosity of the coating color. The substrate Reynolds number is defined as $Re_s = U_s W\rho/\mu$, and $Fr = U_s/\sqrt{gW}$ is the Froude number.

One of the difficulties in solving Eqs. 1–3 is the absence of a direct relationship between the pressure and the divergence-free constraint imposed by the continuity equation. Attempts to enforce continuity (Eq. 3) at each time throughout the flow field give rise to nonlinear instabilities in the momentum equations (Eqs. 1 and 2). It has been established that such a connection is introduced when the continuity equation (Eq. 3) is replaced by the Poisson pressure equation, which is derived from Eqs. 1 and 2:

$$\frac{\partial^2 p}{\partial x^2}+\frac{\partial^2 p}{\partial y^2}=-\frac{\partial}{\partial x}\left(\frac{\partial u^2}{\partial x}+\frac{\partial uv}{\partial y}\right)-\frac{\partial}{\partial y}\left(\frac{\partial uv}{\partial x}+\frac{\partial v^2}{\partial y}\right)-\frac{\partial D}{\partial t}, \tag{4}$$

where $D = \partial u/\partial x + \partial v/\partial y$ is the dilation.

Boundary conditions

Boundaries of the flow region in the short-dwell coater can be divided into three categories: the solid-wall boundaries, inlet or outlet boundaries, and free-surface boundaries.

The boundary conditions along all the solid walls except the two dynamic contact points express the no-slip hypothesis of the theory of fluid mechanics. In equation form this hypothesis expresses the equality of the fluid velocity at the solid wall to the velocity of the solid wall. With reference to Figure 1b, the boundary conditions in dimensionless form are

$$\begin{aligned}
u=1,\quad v=0 \quad &\text{for} \quad y=1, \quad x_d<x\le 3\\
u=1,\quad v=0 \quad &\text{for} \quad y=1, \quad x_d<x\le 3\\
u=0,\quad v=0 \quad &\text{for} \quad y=x, \quad 0\le x\le 0.875\\
y=0.875,&\quad 0.875\le x\le 1\\
x=1,&\quad 0\le y\le 0.875\\
y=0,&\quad 1\le x\le 1.425\\
y=0,&\quad 1.575\le x\le 2\\
x=2,&\quad 0\le y\le 1-\lambda-0.1\tan(\alpha)\\
y=1-\lambda-(2.01-x)\tan(\alpha),&\quad 2\le x\le 2.01.
\end{aligned} \tag{5}$$

At the inlet boundary, the inlet flow is assumed to be a plug flow. The velocity is determined by the coating gap, L_c, substrate Reynolds number, Re, and the recirculation ratio, S_r. The initial velocity condition at the inlet boundary is calculated as

$$u = 0, \quad v = Q_i/L_i = Q_i/0.15 \quad \text{for} \quad y = 0, \quad 1.425 \le x \le 1.575, \tag{6}$$

where $Q_i = (S_r + 1)Q_c = (S_r + 1)\int_{1-L_c}^{1} u dy$.

At the outlet, the velocity boundary conditions are assumed to be continuous with a constant gradient, and the continuity principle applies.

$$\partial^2 u/\partial x^2 = 0 \quad \partial u/\partial x + \partial v/\partial y = 0 \quad \text{for} \quad x = 3,$$
$$(1 - L_f) \le y \le 1 \qquad y = -x, \quad -\delta\cos(\beta) \le x \le 0, \tag{7}$$

where δ is the overflow film thickness and β is the angle of inclination of the overflow plate.

The pressure boundary conditions for both the solid-wall and inlet/outlet boundaries are the Neumann pressure boundary conditions (Abdallah, 1987), which can be easily derived from the momentum equations (Eqs. 1 and 2) by substituting the continuity equation into the viscous terms of the momentum equations:

$$\frac{\partial p}{\partial x} = -\frac{\partial u^2}{\partial x} - \frac{\partial uv}{\partial y} - \frac{1}{Re}\frac{\partial \omega}{\partial y} \tag{8a}$$

$$\frac{\partial p}{\partial y} = -\frac{\partial uv}{\partial x} - \frac{\partial v^2}{\partial y} + \frac{1}{Re}\frac{\partial \omega}{\partial x} - \frac{1}{Fr^2} \tag{8b}$$

where

$$\omega = \frac{\partial v}{\partial x} - \frac{\partial u}{\partial y}.$$

At the free surface, there are four unknowns, u, v, p, and the free surface profile $y(x)$. Four independent boundary conditions are needed. They are the normal and shear-stress balance conditions, the continuity equation, and the kinematic condition.

The normal and shear-stress balance equations on the free surface can be found in Esmail and Hummel (1975) in the dimensionless form:

$$-2b\frac{\partial u}{\partial x} + \frac{\partial u}{\partial y} + \frac{\partial v}{\partial x} + bRe\left(p - p_0 + \frac{1}{WeR}\right) = 0 \tag{9a}$$

$$2\frac{\partial v}{\partial y} - b\left(\frac{\partial u}{\partial y} + \frac{\partial v}{\partial x}\right) - Re\left(p - p_0 + \frac{1}{WeR}\right) = 0, \tag{9b}$$

where

$$b = dy(x)/dx,$$

the Weber number $We = \rho U_s^2 W/\sigma$, and

$$\frac{1}{R} = \frac{db/dx}{(1 + b^2)^{3/2}},$$

σ is the coating color surface tension.

Equations 9a and 9b are projections of the dynamic stress balance onto a direction tangential to the free surface, and a direction normal to the surface. They were made dimensionless by introducing the substrate velocity U_s, the width of the coating pond W, and the density of the fluid ρ.

At the free surface, the continuity equation must be satisfied.

$$\partial u/\partial x + \partial v/\partial y = 0 \tag{9c}$$

The free surface is a natural streamline. Therefore, the following kinematic condition, which expresses a mass balance across the film, must be satisfied.

$$dy/dx = v/u. \tag{9d}$$

There is a stagnation point on the overflow free surface. There the two components of velocity u and v vanish. Then Eq. 9d becomes undetermined. Therefore, on the overflow section of the free surface we can use another kinematic condition expression introduced by Thompson (1980):

$$\left(\frac{\partial y}{\partial t}\right)_x = v - u\left(\frac{\partial y}{\partial x}\right)_t. \tag{9e}$$

These equations are used to find the velocity on the free surfaces. The normal stress-balance equation is used to calculate the pressure on the free surface. The free-surface profile is updated according to Eq. 9d or Eq. 9e.

Equations 1 and 2 and Eq. 4, with the appropriate boundary conditions from Eqs. 5–9, are transferred into the curvilinear coordinates by elliptic numerical transformations, as described by Vinokur (1974).

Curvilinear numerical grid generation

The numerical grid generation technique is used to transform the irregular physical domain to a regular computational domain. In general, numerical grids could be generated either by algebraic interpolation methods or by partial differential equations methods. Grids could be generated either by elliptic, parabolic, or hyperbolic partial differential equations. We used the elliptic partial differential equation method. There are two main objectives in using the numerical curvilinear grid generation. First it can transform any complex physical domain into a regular computational domain. In addition it can also give us direct control over the distribution of grid points in the physical domain. By adopting this numerical grid generation technique, we can design certain grid distributions that suit the vastly different scales present in our problem.

The Poisson equations used in the generation of the grid are those proposed by Thomas and Middlecoff (1980). The remarkable aspect of these elliptic grid generators is that the grid-point distribution inside the domain is directly controlled by point distributions on the boundaries. This transformation ensures a one-to-one correspondence of points, and that values of the control function at all internal points are calculated from the boundary distributions. For a two-dimensional domain, the Poisson equations used to transform from

the (x, y) physical domain to the (ζ, η) computational domain are

$$\alpha(x_{\zeta\zeta} + \phi x_\zeta) - 2\beta x_{\zeta\eta} + \gamma(x_{\eta\eta} + \psi x_\eta) = 0$$
$$\alpha(y_{\zeta\zeta} + \phi y_\zeta) - 2\beta y_{\zeta\eta} + \gamma(y_{\eta\eta} + \psi y_\eta) = 0 \qquad (10)$$

where

$$\alpha = x_\eta^2 + y_\eta^2$$
$$\beta = x_\zeta x_\eta + y_\zeta y_\eta$$
$$\gamma = x_\zeta^2 + y_\zeta^2$$
$$\phi = -(x_\zeta x_{\zeta\zeta} + y_\zeta y_{\zeta\zeta})/(x_\zeta^2 + y_\zeta^2) \quad \text{on} \quad \eta = \eta_b$$
$$\psi = -(x_\eta x_{\eta\eta} + y_\eta y_{\eta\eta})/(x_\eta^2 + y_\eta^2) \quad \text{on} \quad \zeta = \zeta_b.$$

The functions used to describe a grid-point distribution on a boundary are commonly called the *stretching functions*. A stretching function can be used in any transformations involving grid stretching or clustering. The so-called optimum stretching functions, which give minimum truncation error in finite difference, are the inverse hyperbolic sine functions and inverse tangent functions, according to Vinokur (1980). Therefore, in our calculation, inverse hyperbolic stretching functions are used to cluster the grid lines toward the top moving substrate in the y direction, and toward the static contact point at the blade tip in x direction.

Treatment of singularity points

Some of the difficulties arising in the simulation of coating flows are associated with static and dynamic contact points, and the coating free surface. The boundary conditions at the free surface were discussed earlier. The static contact point (point B in Figure 1a) is a singularity point according to the theory of fluid dynamics. As Ames (1978) indicated, finite difference computations give "infected results" in the vicinity of a singularity point. He also indicated that one of the effective ways to remove this "infection" is to use finer grids. In order to reduce the adverse effect of this singularity, a hyperbolic sine-stretching function is adopted in the numerical grid generation technique. The purpose is to concentrate the grid lines in the vicinity of the singularity point. The flow under the blade is driven by the high-speed substrate. This leads (Leung and Esmail, 1987) to minimum exit effects in the vicinity of this point. Therefore, for paper coating with very high velocities, it is reasonable to assume no slip at this static contact point. Boundary conditions on the coating free surface, and the treatment for the static contact point have been tested in a separate study (Cao, 1993).

The presence of a dynamic contact point where the substrate first comes in contact with the coating color adds a serious complication to the numerical simulation of the flow. On the overflow free surface there is also a stagnation point (Figure 1b). The boundary conditions at these two points are much more complicated than those at the static contact point discussed earlier.

The difference between the static and dynamic contact points lies in the mathematical nature of stress distributions in the immediate neighborhood of these points. At the static contact point there is a stress singularity that is inversely proportional to the square root of the distance from the static contact point. This singularity is integrable: the total force on the solid wall is finite (Kistler and Scriven, 1983). At dynamic contact points, the stress singularity arising from the no-slip condition is not integrable: conventional fluid mechanics predicts an unbounded force about the wetting line. That is to say, although the no-slip condition is not applicable at both static and dynamic contact points, the use of the no-slip condition at a static contact point is still theoretically possible. The problem then was to minimize or eliminate the infection propagating from the singularity. The no-slip condition cannot be used in the case of dynamic contact points, because the unbounded force it induces leads to mathematical and numerical instabilities, which destroys the possibility of arriving at any solution.

Kistler and Scriven (1983) suggested two ways to treat the dynamic contact point in numerical simulations. One way is to use experimentally determined values of the contact angle. The other is to assume that velocity components at the dynamic contact point are zeros. In their words, the dynamic contact point always consists of the same material point. These conditions were applied to problems with low capillary numbers, $Ca = \mu U_s/\sigma$. In most other numerical studies, experimental values of the dynamic contact angle are prescribed as a given boundary condition. The dynamic contact angle has been under intensive studies. Ghannam and Esmail (1990) found that the dynamic contact angle is dependent on liquid properties, flow parameters, and substrate geometry. Dynamic contact angles measured in a particular system are specific to this system, and may not be valid values for a different system, even if the same liquid and substrate materials were used.

It has been suggested by many authors (Blake, 1988) that at high capillary numbers the dynamic contact angle is primarily influenced by the hydrodynamic forces of the flow. At lower capillary numbers interfacial surface tension and other surface energy parameters have a significant effect on the formation of a contact angle. Since our problem in short-dwell coating is in the range of high capillary numbers, we can reasonably assume that the dynamic contact angle is primarily formed by the hydrodynamic forces.

At the dynamic contact point, the no-slip condition of theoretical fluid mechanics is no longer valid. We assumed that there is a certain amount of slip at the dynamic contact point. Therefore, the velocity at this point is not identical to that of the solid substrate. It is assumed that the velocity component vertical to the substrate is zero. The velocity component tangential to the moving substrate is linearly extrapolated from the numerically obtained velocity distribution along the free surface. In effect, the amount of slip at the contact point is determined by the hydrodynamic forces that shape the free surface.

Consideration of the flow configuration in the overflow section indicates the presence of a stagnation point on the overflow free surface. The boundary condition used to calculate the free-surface profile, which we called the kinematic condition $dy/dx = v/u$, cannot be used at this point, due to its singular nature. At the stagnation point, the two velocity components are zeros. Then the term dy/dx in the kinematic

condition becomes undefined. According to Thompson (1980), the free-surface profile can be described by the function $y = f(x,t)$. This can be rewritten as $f(x,t) - y = 0$. Then the convective derivative of this function must vanish.

$$\frac{d}{dt}[f(x,t) - y] = 0.$$

We can then write

$$\frac{d}{dt}[f(x,t) - y] = \left(\frac{\partial f}{\partial t}\right)_x + \left(\frac{\partial f}{\partial x}\right)_t \frac{dx}{\partial t} - \frac{dy}{dt} = 0.$$

By substituting $y = f$, $dy/dt = v$, and $dx/dt = u$, we will have

$$\left(\frac{\partial y}{\partial t}\right)_x = v - u\left(\frac{\partial y}{\partial x}\right)_t.$$

This is the boundary condition we used to calculate the free-surface profile in dynamic contact angle calculations.

The processes and liquid physical properties are described in our calculations by three dimensionless groups. The Reynolds number, $Re = \rho W U_s/\mu$, capillary number, $Ca = \mu U_s/\sigma$, and the Froude number, $Fr = U_s/\sqrt{Wg}$. These three dimensionless groups define the relative importance of the inertial, viscous, surface tension and the gravity forces.

In conclusion, the value of the dynamic contact angle was numerically simulated. Three assumptions were used in the development of this procedure: (1) a limited slip at the dynamic contact point; (2) the velocity component vertical to the substrate at this point is set to zero; (3) the velocity tangential to the substrate at this point is set to a linearly extrapolated value from the corresponding values on the free surface. The slope of the free surface profile in the vicinity of the dynamic contact point is also linearly extrapolated from the dynamic contact angle, and to produce the location of the wetting point. The method is applicable at higher capillary numbers, corresponding to a range of speeds, where hydrodynamic forces dominate the wetting phenomena on the macroscopic scale.

Initial conditions

The initial conditions in simulating the flow in a short-dwell coater have some influence on the computer time used. The rates of solution convergence are most sensitive to the initial conditions in flow sections with free surfaces. In this article, the analytical solutions of the falling film flow discussed earlier are supplied as initial conditions for overflow free-surface flow. Meanwhile, the Nusselt flow velocities are supplied as initial conditions for the free-surface coating section of the flow. Zero velocities are used as initial conditions for all other sections of the flows. The pressure initial conditions for all the domain are set to zero. The procedures of the solution are summarized in Figure 2.

Results and Discussion

Numerical calculations have been performed for various combinations of the operating variables. The four parameters

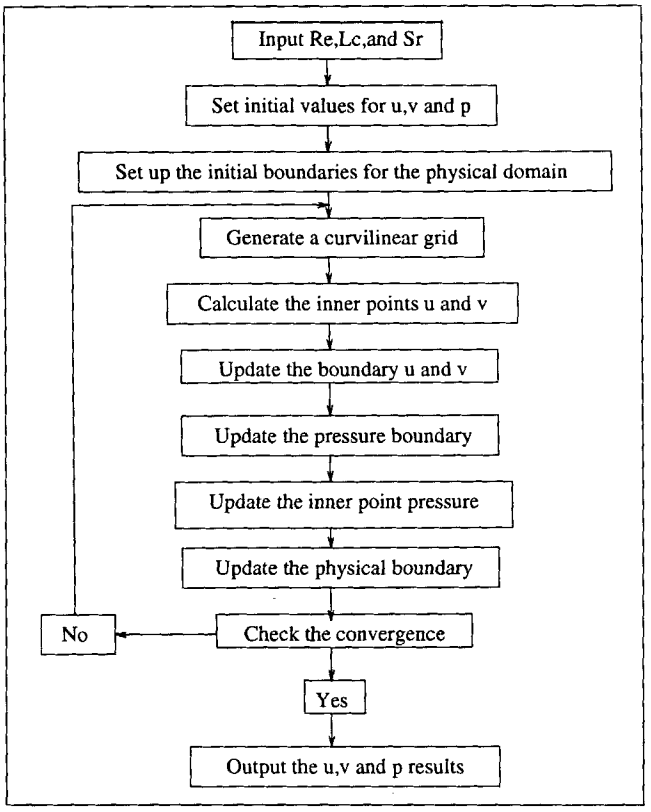

Figure 2. Computational scheme.

used in calculations are the substrate Reynolds number Re, the recirculation ratio S_r, the coating gap L_c, and the blade angle α. The effects of these four parameters on the velocity, pressure, centrifugal force, and shear rate distributions will be discussed. Moreover, the effects of the hydrodynamic flow in short-dwell coaters on the properties of the coated products will also be discussed. It will be made clear that hydrodynamic parameters of the short-dwell coaters may be responsible for the inducement of poorer quality of products. All the calculations are performed in dimensionless form. Parameters in the dimensional form were calculated using the following values of the design variables (Figure 1b for definitions): coating pond width $W = 0.04$ m; coating pond depth $D = 0.04$ m; coat baffle gap $L_0 = 0.005$ m; blade thickness $L_b = 0.0004$ m; inlet opening $L_i = 0.005$ m; and blade angle $\alpha = 0$–$20°$. The coating color viscosity and density were assumed to be $\mu = 1$ Pa·s, and $\rho = 1{,}400$ kg/m^3, respectively.

Flow patterns

The complete picture of flow patterns inside and around the short-dwell coaters can only be obtained by simulating the flow in and around the coater simultaneously as we did here. Descriptions of flow patterns in a short-dwell coater are shown in Figure 3. The complete flow-pattern picture is obtained for the short-dwell coating processes. It is clear that inside the coating pond there is a main vortex that dominates the flow. There are as many as four secondary vortices present in the flow region. The two secondary vortices inside the coating pond were seen in our previous study (Cao and Esmail, 1992). The other two vortices can only be seen by in-

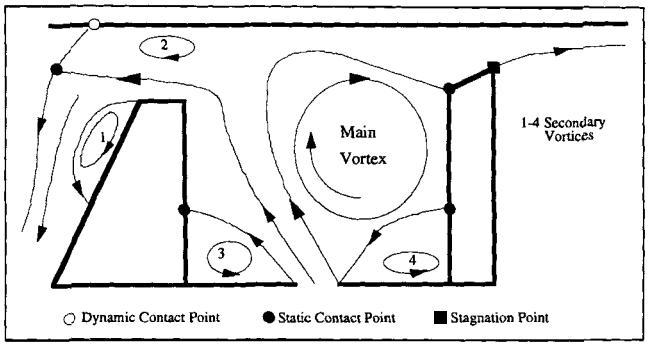

Figure 3. Velocity flow patterns in a short-dwell coater.

cluding the overflow free-surface section in the domain of simulation. We found that there is a secondary vortex right under the dynamic contact point, where the moving substrate starts its contact with the outcoming overflow coating color. The other secondary vortex on the overflow section is located on the top of the inclined plate. The size of this vortex increases with increases in the substrate Reynolds number, *Re*, as shown in Figure 4. In comparison with the effects of the substrate Reynolds number, the effects of the other parameters on flow patterns are rather insignificant. As we expected, there is a stagnation point on the overflow free surface. The position of this stagnation point moves up toward the dynamic contact point as the substrate Reynolds number increases, and down away from the dynamic contact point when the substrate Reynolds number decreases. Inside the coating pond there is another stagnation point at the blade tip.

The effects of the main and secondary vortices on the stability of operation and product quality are very important.

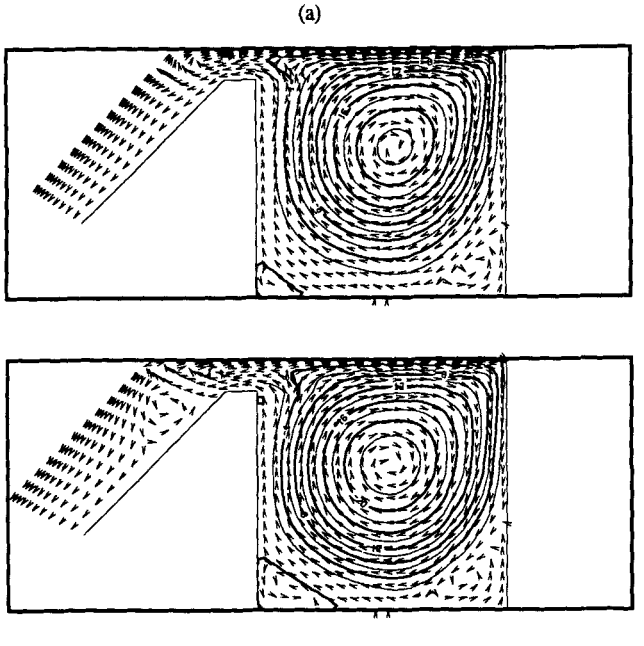

Figure 4. Complete velocity flow patterns in and around a short-dwell coater.

$S_r = 20$, $L_c = 0.001$, and $\alpha = 10°$. (a) $Re = 400$; (b) $Re = 1{,}200$.

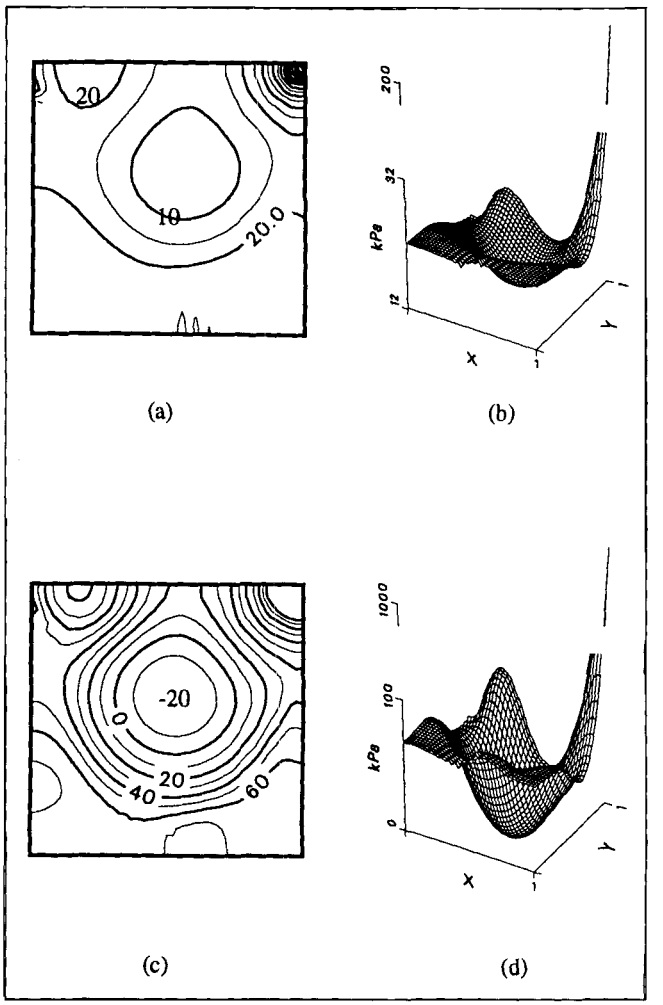

Figure 5. Pressure distributions inside the coating ponds.

$S_r = 20$, $\alpha = 20°$, and $L_c = 0.0005$. (a) Pressure contours at $Re = 400$; (b) three-dimensional surface of pressure at $Re = 400$; (c) pressure contours at $Re = 1{,}200$; and (d) three-dimensional surface of pressure at $Re = 1{,}200$.

Significant influence is exercised by the main vortex and the secondary vortex right under the dynamic contact point. As we will discuss later, these two vortices induce a random orientation distribution of pigment particles during operation. *This will produce a coating layer on the substrate with lower surface strength and gloss.* It must be noted that the capillary number of the coating operation in a short-dwell coater is usually high. There is a very good chance that air entrainment will occur at the dynamic contact point. Moreover, because of the existence of the secondary vortex under the dynamic contact point, any instability or disturbance induced by air entrainment or other possibility will result in flow fluctuations, which will have an unfavorable effect on the product quality.

Pressure distributions

The pressure distribution in a short-dwell coater is shown in Figure 5. Although there are no negative pressure zones

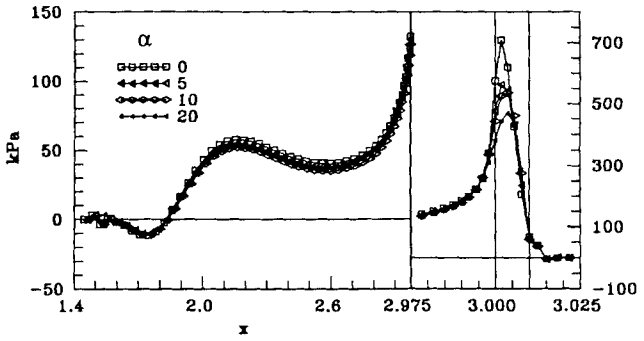

Figure 6. Pressure distributions on the substrate surface for different blade angles.

$Re = 600$, $S_r = 20$, and $L_c = 0.001$.

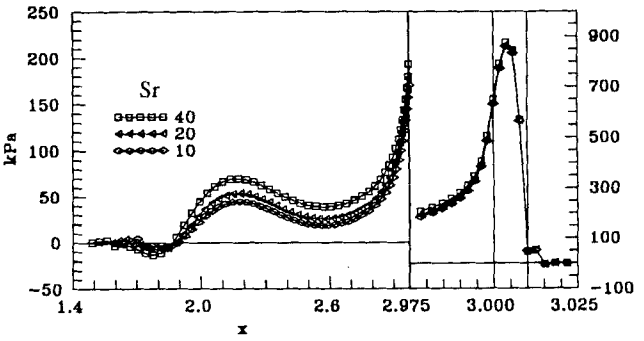

Figure 8. Pressure distributions on substrate surface for different recirculation ratios.

$Re = 800$, $L_c = 0.001$, and $\alpha = 10°$.

inside the coating ponds at lower Reynolds number ($Re < 800$), there is always a minimum pressure zone at the center of the coating ponds. For $Re = 400$, the minimum pressure value is about 10 kPa. This indicates that *at any Reynolds numbers, if air is entrained into the system, the entrained air will be concentrated at this minimum pressure zone inside the pond.* It is necessary to remove air by vacuum from the center of the pond only at high Reynolds numbers, since only then could there be a negative pressure zone.

Pressure distributions over the substrate surface are an important factor in liquid penetration and migration during coating color application. The effects of the four control parameters in our simulation on pressure distributions over the substrate are shown in Figures 6 to 9. Before we start our discussion, let us note a few important locations on the x coordinate. The first important location is the dynamic contact point, where the coating color initiates its contact with the substrate. The location $x = 2.0$ is the upstream corner of the coating pond, where the pressure was set to zero, as indicated in the previous section. The position $x = 3.0$ is the downstream corner of the coating pond, which is the upstream tip of the blade. Position $x = 3.01$ is the downstream tip of the blade.

Blade angles, defined in Figure 1b, have almost no effect on pressure distributions over the substrate surface upstream from the inside blade tip, as shown in Figure 6 when $x \leq 3.0$. Blade angles have a notable effect on pressure distributions under the blade, that is, $3.0 \leq x \leq 3.01$. There is a maximum pressure under the blade. Its value increases as the blade angle decreases. Its location moves downstream as the blade angle increases. It is also clear that the pressure at the point $x = 2.0$ has a positive value. Upstream of $x = 2.0$, there is a minimum pressure, which has a negative value.

Coating gaps, which control the coating weight, have a significant effect on pressure distributions over the substrate surface both upstream and downstream of the blade (Figure 7). Lower coating weights, corresponding to lower coating gaps, always lead to higher pressures on the substrate. The location of maximum pressure under the blade ($3.0 \leq x \leq 3.01$) does not change with coating gaps, although the value of this maximum varies with gaps.

The recirculation ratios, which are defined as ratios of the flow rates of the overflow to the coating flow, have almost no effect on pressure distributions under the blade ($3.0 \leq x \leq 3.01$). But they have notable effect on the pressure inside the coating pond and further upstream. It is also found (Figure 8) that the dynamic contact point moves further upstream as the recirculation ratio increases. The pressure at $x = 2.0$ also increases as the recirculation ratio increases.

The other parameter that affects pressure distributions over the substrate surface is the substrate Reynolds number. Figure 9 shows that the pressure increases in all points over the substrate surface for higher substrate Reynolds numbers. The maximum pressure increases from about 300 kPa at $Re = 400$ to about 1,700 kPa at $Re = 1{,}200$. This is to say, *the maximum pressure is proportional to the substrate Reynolds number raised*

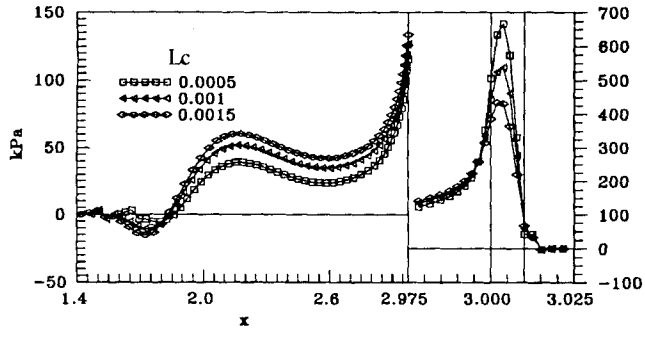

Figure 7. Pressure distributions on substrate surface for different coating gaps.

$Re = 600$, $S_r = 20$, and $\alpha = 10°$.

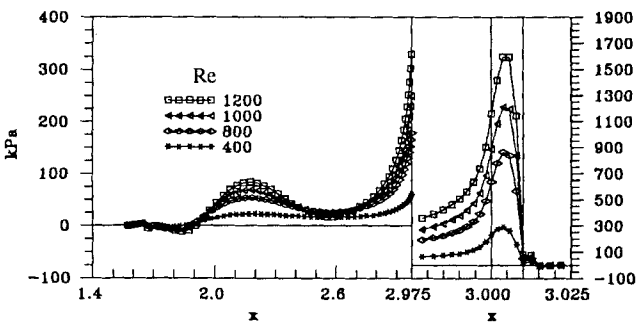

Figure 9. Pressure distributions on substrate surface for different Reynolds numbers.

$S_r = 20$, $L_c = 0.0005$, and $\alpha = 20°$.

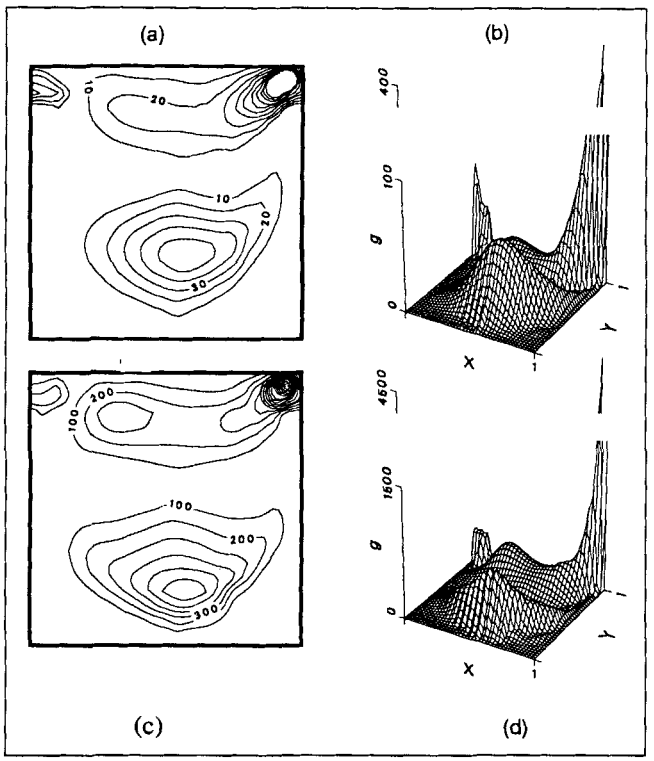

Figure 10. Centrifugal force distributions inside the short-dwell coating ponds.

$S_r = 20$, $L_c = 0.0005$, and $\alpha = 20°$. (a) Contours at $Re = 400$; (b) three-dimensional surface of centrifugal force at $Re = 400$; (c) contours at $Re = 1{,}200$; and (d) three-dimensional surface of centrifugal force at $Re = 1{,}200$.

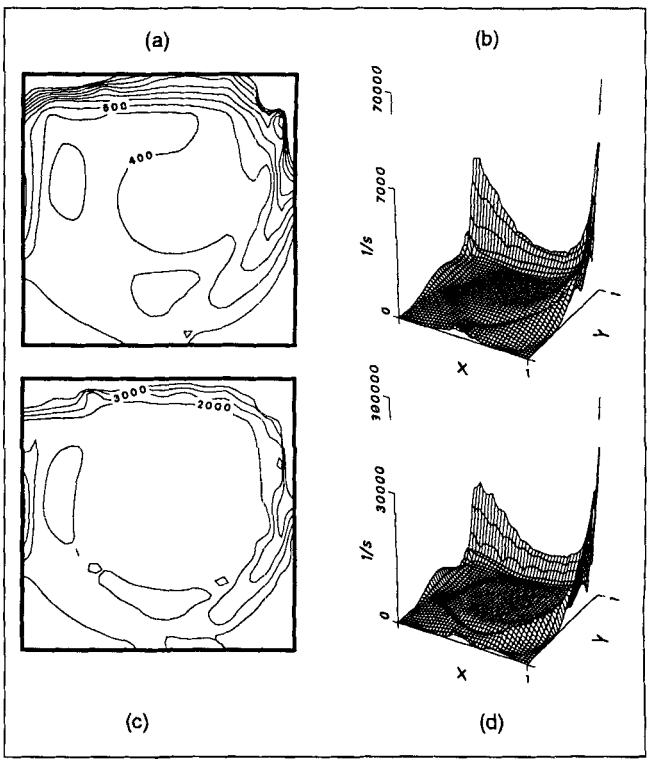

Figure 11. Shear rate distributions inside short-dwell coating ponds.

$S_r = 20$, $L_c = 0.0005$, and $\alpha = 20°$. (a) Contours of shear-rate distribution for $Re = 400$; (b) three-dimensional surface distribution of shear rate for $Re = 400$; (c) contours of shear rate at $Re = 1{,}200$; and (d) three-dimensional surface of shear rate at $Re = 1{,}200$.

to a power higher than unity. The other important result is that the pressure on the substrate is negative only upstream of the coating pond. *The substrate surface pressure inside the coating pond* ($2.0 \le x \le 3.0$) *is always positive*. In our previous studies (Cao and Esmail, 1992), the pressure did have a negative value at high Reynolds numbers. This was due to the assumption of zero pressure at the point $x = 2.0$. This reminds us once again that the correct absolute value of pressure can only be obtained by the simultaneous simulation of the complete flow domain. The most significant effect on pressure distributions over the substrate surface is offered by the substrate Reynolds number. Coating gaps, blade angles, and recirculating ratios have fewer effects in the stated order of significance.

Distributions of centrifugal forces

The inclusion of the overflow free surface in the numerical simulation does improve the velocity and pressure results as discussed earlier. However, flow patterns inside the coating pond are not affected by the overflow region. Subsequently, distributions of centrifugal forces inside the coating pond are also independent of the overflow patterns. In order to improve our understanding of the effect of hydrodynamics on the properties of coated paper, distributions of centrifugal forces at two different Reynolds numbers are shown in Figure 10. There are always two maximum centrifugal force zones inside the coating pond: the maximum values in the bottom maximum zone increase from about 60 g at $Re = 400$ to about 600 g at $Re = 1{,}200$, while the maximum values in the top zone increase from about 400 g at $Re = 400$ to about 4,500 at $Re = 1{,}200$. Although the action of these maximum zones on particles occurs over a very short time period due to the particles' speeds, *this extremely high centrifugal force will change the path of large particles and divert them from the streamline they were supposed to follow*.

Distributions of the shear rate

As with the centrifugal forces, shear rates are dependent on the velocity field. Since velocity fields inside the pond did not experience significant changes when the overflow free surface was added to the numerical simulation, distributions of shear rates inside the pond did not change. The shear stress, which is proportional to the shear rate for Newtonian fluids, is considered to have some effect on particle orientation in the coating layer. By presenting the shear-rate distributions inside the coating ponds at two different Reynolds numbers, we show that a very low shear zone is located in the center of the coating pond. Figure 11 shows the shear rates at $Re = 400$ and 1,200. In the case of $Re = 1{,}200$, the maximum shear rate is about 3×10^5/s inside the coating pond. We found that this high shear is encountered only inside a very thin layer adjacent to the substrate. The center of the pond, where the main vortex is located, is under very low shear (lower than 2,000/s for $Re = 1{,}200$). *This low shear zone*

combined with the circulating motion of the main vortex, will induce random orientations of the solid pigment particles in the coating color. This will result in a poorer coating quality compared to the roll-applicator blade coaters.

Conclusions

A simulation of the flow in a short-dwell paper-coating process, which simultaneously treats the flow inside the coating pond, the flow under the blade, the coating free-surface flow, and the recirculation flow, is achieved for the first time. By including the two sections of free surfaces into the simulation domain and applying the consistent Neumann boundary conditions to the pressure Poisson equation, a pressure field, which is unique and absolutely determined, is obtained.

Numerical results show that velocity patterns inside the short-dwell coating pond are complicated by one main vortex and up to four secondary vortices. The main vortex and the secondary vortex by the dynamic contact point induce a random orientation distribution of pigment particles during operation. The random orientation of particles will produce a coating layer on the substrate, with lower surface strength and gloss. Distributions of shear rate indicate that its value is very high only in the vicinity of the substrate. A low shear zone at the center of the pond assists the circulating motion of the main vortex in inducing the random orientation of solid pigment particles in the coating color.

Coating gaps have a significant effect on pressure distributions over the substrate surface, both upstream and downstream of the blade. There is a maximum pressure under the blade, and its value increases with increases in the substrate Reynolds number and with decreases in coating gaps and blade angles. Recirculation ratios have almost no effect on pressure distributions under the blade. The maximum pressure is proportional to the substrate Reynolds number raised to a power higher than unity. The pressure on the substrate is negative only upstream of the coating pond. And substrate surface pressure inside the coating pond is always positive.

Centrifugal force distributions show that there are two high centrifugal force zones inside the coating pond. These zones will change the path of large particles and divert them from the streamlines they were supposed to follow. As a result, they may be a source of coating flow instability and coating defects.

A newly proposed finite-difference scheme combined with the body-fitted coordinates technique, and coupled with the implementation of grid clustering, proved to be a successful method in simulating a flow problem with vastly different scales in different flow regions. This technique could be applied to other problems with vastly different scales. The proposed treatment of singularity points, the static and dynamic contact points, was effective and reasonably accurate, reflecting the physical phenomena in the range of the assumptions made.

Notation

Fg = relative centrifugal force, defined by Eq. 12
g = gravity constant, m/s^2
H = depth of the pond, m
L_d = overflow film thickness, m
L_f = final coating layer thickness, m
p = pressure, dimensionless
p_0 = atmospheric pressure, Pa
Q_c = coating flow rate, m^2/s
Q_i = inlet flow rate, m^2/s
Q_r = recirculation flow rate, m^2/s
R = radius of curvature on streamline, m
t = time, dimensionless
$\bar{x}$ = physical coordinate, m
x_d = location of dynamic contact point, m
$\bar{x}_d$ = location of dynamic contact point, dimensionless
$\bar{y}$ = physical coordinate, m

Greek letters

λ = overflow film thickness, dimensionless
ω = vorticity, defined by Eq. 10
δ = thickness of overflow film, dimensionless

Literature Cited

Abdallah, S., "Numerical Solutions for the Pressure Poisson Equation with Neumann Boundary Conditions Using a Non-Staggered Grid," *J. Comput. Phys.*, **70**, 182 (1987).

Ames, W. F., *Numerical Methods for Partial Differential Equations*, Academic Press, New York, p. 230 (1977).

Blake, T. D., "Wetting Kinetics—How Do Wetting Lines Move?," paper presented at the AIChE Meet., New Orleans, LA (Mar. 7–10, 1988).

Cao, Z., "A Numerical and Experimental Study on Hydrodynamics of Short-Dwell Paper Coaters," PhD Thesis, Univ. of Saskatchewan, Saskatoon, Sask., Canada (1993).

Cao, Z., and M. N. Esmail, "Numerical Simulation of Short-Dwell Coaters: Steady State Flow Patterns and Pressure Distributions," *Can. J. Chem. Eng.*, **70**, 654 (1992).

Esmail, M. N., and R. L. Hummel, "Nonlinear Theory of Free Coating Onto a Vertical Surface," *AIChE J.*, **21**, 958 (1975).

Ghannam, M. T., and M. N. Esmail, "Effect of Substrate Entry Angle on Air Entrainment in Liquid Coating," *AIChE J.*, **36**(8), 1283 (1990).

Kistler, S. F., and L. E. Scriven, "Coating Flows," *Computational Analysis of Polymer Processing*, J. R. A. Pearson and S. M. Richardson, eds., Applied Science, London, UK (1983).

Kurath, J. S., "Viscosity of Coating Colors at High Shear Rates," TIS 0110-02, TAPPI Technical Information Sheets, Vol. 1, TAPPI Press, Atlanta, GA (1992).

Leung, S. K.-L., and M. N. Esmail, "Velocity Profiles at the Exit of Circular Tubes," *Can. J. Chem. Eng.*, **65**, 3 (1987).

McDermott, M. D., "Operating Experiences: Beloit Short Dwell Coater," *Pulp Paper Can.*, **87**(12), 172 (1986).

Pentti, J. R., and S. T. Luomi, "High-Speed Coating Processes: Trends and Developments," *TAPPI J.*, **67**(12), 46 (1984).

Renvall, S. V., P. J. Rantiainen, and J. C. Rossitto, "Optimizing the Coating Process for Double Coated Woodcontaining Papers," *Proc. TAPPI Coating Conf.*, 339 (1990).

Sollinger, H.-P., "Dynamic Coater—seine Auftrags—und Egalisiersysteme," *Wochenbl. Papierfab.*, **8**, 332 (1989).

Thomas, P. D., and J. F. Middlecoff, "Direct Control of Grid Point Distribution in Meshes Generated by Elliptic Equations," *AIAA J.*, **18**(6), 652 (1980).

Thompson, J. F., "Numerical Solution of Flow Problem Using Body-Fitted Coordinate Systems," *Computational Fluid Dynamics*, W. Kollmann, ed., Hemisphere, Washington, DC (1980).

Triantafillopoulos, N. G., G. R. Rudemiller, T. Farrington, Jr., and J. Lindsay, "Numerical Simulation of Short-Dwell Coater Pond Flows," *TAPPI Engineering Conference Proceedings*, Book 1, Chicago, p. 409 (Sept. 20–22, 1988).

Vinokur, M., "Conservation Equations of Gas-Dynamics in Curvilinear Coordinate Systems," *J. Comput. Phys.*, **14**, 1105 (1974).

Vinokur, M., "On One-Dimensional Stretching Functions for Finite-Difference Calculations," *J. Comput. Phys.*, **50**, 215 (1983).

Wight, E. W., "Modern Coating Application and Blade Metering Systems," paper presented at the TAPPI Blade Coating Seminar, TAPPI Press, Atlanta (1988).

Manuscript received July 7, 1994, and revision received Sept. 28, 1994.